energies

MDPI

*Article*

# Optimization and Predictive Correlation of Thermal-Hydraulic Performance for Transcritical Methane in an Airfoil-Fin Printed Circuit Heat Exchanger

**Changyu Sun [1], Xiaolin Ma [1], Yaxin Zhang [1], Lin Li [2], Jianzhong Yin [1,2,*] and Tao Yang [1,*]**

[1] School of Chemical Engineering, Xinjiang University, Urumqi 830046, China; cysun2017@126.com (C.S.); 18167955726@163.com (X.M.); 13619903328@163.com (Y.Z.)
[2] School of Chemical Engineering, Dalian University of Technology, Dalian 116024, China; li_lin97@126.com
* Correspondence: jzyin@dlut.edu.cn (J.Y.); xju_yt@163.com (T.Y.)

## Abstract

This study investigates the flow and heat transfer characteristics within a printed circuit heat exchanger (PCHE) equipped with airfoil fins. A numerical model of a counter-flow airfoil-fin PCHE was developed, using transcritical methane as the cold medium and a 50 wt% ethylene glycol aqueous solution (50% EGWS) as the hot medium. The effects of the airfoil fin array longitudinal staggering ratio (*Ks*), transverse pitch ratio (*Kb*), and longitudinal pitch ratio (*Ka*) on the thermal-hydraulic performance of the PCHE were systematically analyzed using the thermal performance factor (*TPF*) for comprehensive evaluation. The optimal configuration was determined to be *Ks* = 0.2, *Kb* = 0.5, and *Ka* = 1.0, achieving a *TPF* up to 1.18 times higher than that of the baseline structure (*Ks* = 1.0). The analysis highlights that aggressive heat transfer enhancement incurs a substantial pressure drop penalty; for instance, reducing *Ka* from 2.0 to 1.0 increases the Nusselt number (*Nu*) by approximately 13%, while simultaneously increasing the Fanning friction factor ($f_{\text{Fanning}}$) by 22%, indicating a significant pressure drop cost. The developed correlations exhibit deviations within ±10% of the simulated values over the Reynolds number (*Re*) range of 8000–25,000, providing a reliable tool for the optimized design of PCHEs.

**Keywords:** printed circuit heat exchanger; transcritical methane; flow and heat transfer characteristics; numerical simulation; airfoil fins; heat transfer correlations

Check for updates

Academic Editor: Gianpiero Colangelo

Received: 22 December 2025
Revised: 18 January 2026
Accepted: 21 January 2026
Published: 22 January 2026

**Copyright:** © 2026 by the authors. Licensee MDPI, Basel, Switzerland. This article is an open access article distributed under the terms and conditions of the Creative Commons Attribution (CC BY) license.

## 1. Introduction

Liquefied natural gas (LNG), a clean fossil fuel, has experienced consistent growth in global consumption to meet rising energy demands [1]. Owing to limitations in constructing coastal onshore LNG terminals, floating storage and regasification units (FSRUs) have emerged as a favorable option for numerous countries and regions [2]. The printed circuit heat exchanger (PCHE), an advanced high-efficiency heat exchanger, exhibits exceptional performance under high-pressure and dynamic sloshing conditions, making it an ideal thermal exchange solution for FSRU applications [3]. In offshore floating platforms employing PCHEs, LNG frequently enters at pressures above its critical point, transitioning into a supercritical state as temperatures increase [4]. Supercritical fluids are characterized by enhanced thermophysical characteristics, including improved diffusivity and thermal conductivity [5]. These features contribute to high performance while significantly reducing pressure losses [6]. Consequently, examining the flow and heat transfer behaviors of supercritical methane ($sCH_4$)

in PCHEs with various channel designs is essential for industrial applications [7]. PCHEs fabricate microchannels through chemical etching, followed by stacking and diffusion bonding of plates via intermolecular adhesion forces. Typically, these flow channels are classified into continuous and discontinuous types [8]. The geometric parameters and channel configurations of PCHEs significantly influence thermal-hydraulic performance [9].

For instance, Zhao et al. [10] conducted numerical investigations on the thermal-hydraulic behavior of supercritical LNG (sLNG) in zigzag-channel PCHEs. They demonstrated how the bend angle, mass flow rate, and inlet pressure influence local heat transfer and pressure drop. Similarly, Cai et al. [11] developed a numerical model of dual-zigzag microchannels employing sLNG as the working fluid, elucidating fundamental transport mechanisms through detailed analyses of key operating parameters such as mass flow rate, temperature, and pressure. Liu et al. [12] numerically examined the heat transfer characteristics of supercritical $CO_2$ ($sCO_2$) in straight vertical channels and PCHEs under both uniformly and non-uniformly heated conditions. The proposed heat transfer correlation for $sCO_2$ exhibited good agreement with experimental results. Jin et al. [13] experimentally investigated the heat transfer characteristics of $sCO_2$ within a zigzag channel PCHE, evaluating its dependence on pressure, temperature, and mass flow rate. The findings indicated that the heat transfer coefficient reaches substantially high levels near the pseudo-critical region owing to pronounced variations in the thermophysical properties of $sCO_2$. Liu et al. [14] investigated the thermal-hydraulic performance of a PCHE precooler within an $sCO_2$ Brayton cycle via numerical simulation and experimental validation. It was observed that wavy channels, by enhancing fluid disturbance, substantially enhance heat transfer efficiency, although this is accompanied by an increased pressure drop. Wang et al. [15] investigated the heat transfer mechanism of sLNG in a U-shaped bend. Considering similarity and safety principles, a nitrogen–argon mixture was used as a surrogate fluid in their experiments. The experimental data obtained with the mixture were employed to validate the accuracy of a numerical model. Simulation results further elucidated the combined effects of centrifugal and buoyancy forces on the heat transfer mechanism. Li et al. [16] numerically investigated the influence of structural parameters on the flow and heat transfer characteristics in a Z-shaped channel PCHE. Their findings indicated that smaller channel diameters and pitches, coupled with larger bending angles, deteriorate flow performance but enhance heat transfer performance. They concluded that the optimal configuration corresponds to a channel diameter of 1.43 mm, a channel pitch of 24.6 mm, and a bending angle of 15°. Ma et al. [17] examined flow and heat transfer mechanisms during the liquefaction process of natural gas within a PCHE, evaluating the impact of sloshing conditions on local friction factors and heat transfer characteristics. Their results showed that sloshing minimally affects the overall heat transfer coefficient in the supercritical natural gas region, whereas it significantly influences the flow characteristics of natural gas near the pseudo-critical region. Tang et al. [18] assessed thermal performance associated with axial heat conduction under varying conditions in Z-shaped channels for sLNG, demonstrating that axial heat conduction significantly affects the thermal performance of the PCHE at low Reynolds numbers. Li et al. [19] predicted the thermal-hydraulic performance of $sCH_4$ flow in a straight channel and proposed an accurate machine-learning-based method.

Park et al. [20] experimentally investigated the comprehensive thermal-hydraulic performance of $sCO_2$ in an airfoil fin PCHE with NACA0020 profiles. The experimental results demonstrated that, for an identical total heat transfer rate per unit volume, the pressure drop in the airfoil fin PCHE was only one-fifth of that in a wavy-channel PCHE. Liu et al. [21] examined the thermal-hydraulic performance of an airfoil fin PCHE using supercritical hydrocarbon fuel and water as working fluids. They proposed correlations for

the Nusselt number and friction factor. Li et al. [22] compared the heat transfer performance of symmetric (NACA0021) and asymmetric (NACA4822) airfoil fins, observing that the fin geometries induce vortex formation during flow. The turbulence intensity generated by these vortices in the asymmetric fin channel was found to enhance temperature distribution and significantly improve heat transfer. Pidaparti et al. [23] developed and implemented an experimental setup incorporating a PCHE with discontinuous fins, systematically analyzing the effects of fin shape, size, and arrangement on the heat exchanger's performance. Their findings indicated that the discontinuous fin design improves the heat transfer coefficient to some degree compared to traditional continuous fins. Arora et al. [24] experimentally investigated the pressure drop and friction factor of an airfoil fin PCHE under various operating conditions. A strong correlation was observed between the pressure drop and the friction factor in the airfoil fin PCHE, with both parameters demonstrating an increasing trend as flow velocity increased. Han et al. [25] experimentally examined the thermal-hydraulic performance of a novel airfoil fin PCHE. Their findings demonstrated that the thermal efficiency of the novel airfoil fin PCHE is substantially higher than that of traditional fin structures. Moreover, the pressure drop of the novel design was also noticeably reduced compared to conventional fin structures.

In summary, investigations into supercritical fluid characteristics within PCHE channels have primarily focused on modifying flow-path geometries to comprehensively characterize their thermal-hydraulic performance. For LNG regasification applications, the thermal transition of $sCH_4$ from −162 °C to ambient temperature occurs across a substantial temperature range, where carefully implemented structural and geometric adaptations substantially influence the overall thermal-hydraulic efficiency [26]. Current research on the thermal-hydraulic behavior of supercritical fluids in PCHEs has predominantly focused on carbon dioxide and nitrogen, with relatively limited attention devoted to $sCH_4$ [27].

The present study investigates the heat transfer characteristics of transcritical methane in counter-flow PCHE channels fitted with airfoil fins. Key parameters examined for their influence on performance include (a) airfoil fin array longitudinal staggering ratio (*Ks*), (b) airfoil fin array transverse pitch ratio (*Kb*), and (c) airfoil fin array longitudinal pitch ratio (*Ka*). Moreover, detailed numerical simulations have facilitated the development of new correlations for predicting the *Nu* and $f_{\text{Fanning}}$ values specific to LNG regasification in PCHEs incorporating NACA0020 airfoil fins.

## 2. Geometry Model of Airfoil-Fin PCHE

The diagrams of the airfoil-fin PCHEs are presented in Figure 1. The PCHE consists of multiple stacked plates, wherein heat exchange occurs between hot and cold fluids in a cross-flow configuration, as shown in Figure 1a. Owing to the periodic configuration [26], the computational domain was reduced to a single pair of counter-flow channels (EGWS and $CH_4$ streams) and the intervening solid domain, as presented in Figure 1b. The PCHEs, which define the computational domain, are composed of several units, each with a length of *Ln*, as depicted in Figure 1c,e. The implementation of periodic boundary conditions in both the streamwise and spanwise directions enabled an accurate representation of the full heat exchanger's performance while simultaneously achieving a substantial reduction in computational effort. The geometric parameters of the airfoil-fin PCHEs are illustrated in Figure 1d.

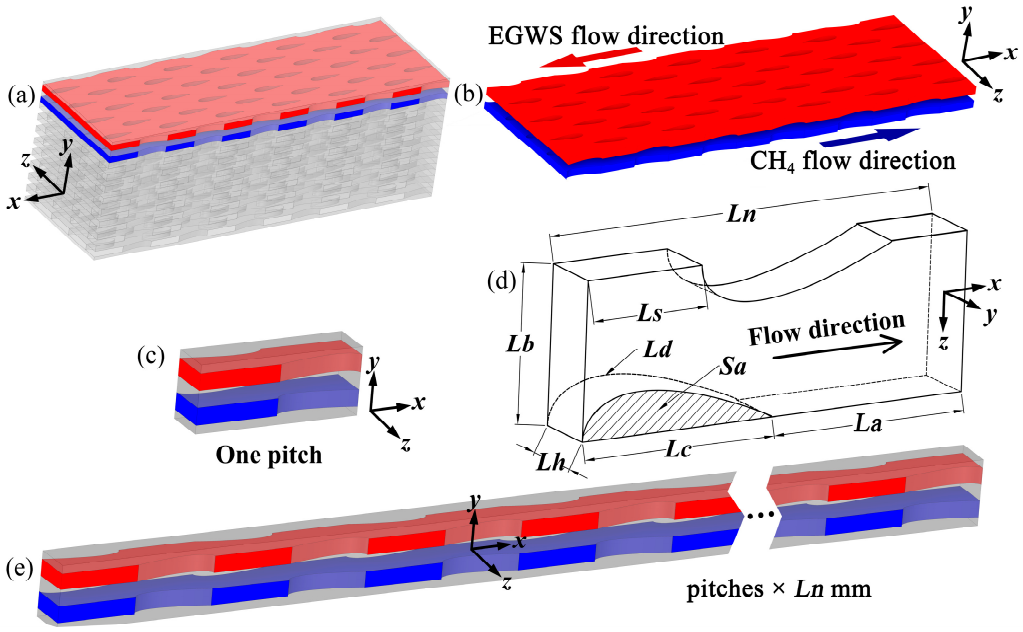



**Figure 1.** Geometric model of the airfoil-fin PCHE: (**a**) PCHE core block; (**b**) counter-flow arrangement of hot and cold streams; (**c**) one pitch; (**d**) key structural parameters; and (**e**) computational domain.

The primary geometric parameters investigated in this study are defined as follows: the longitudinal staggering ratio of the airfoil fin array (*Ks*), the airfoil fin array transverse pitch ratio (*Kb*), and the airfoil fin array longitudinal pitch ratio (*Ka*). The corresponding dimensional parameter values are presented in Table 1.

$$Ks = \frac{Ls}{0.5Ln} \tag{1}$$

$$Ka = \frac{La}{Lc} \tag{2}$$

$$Kb = \frac{Lb}{Lc} \tag{3}$$

**Table 1.** Structural parameters of the geometric model.

| Symbol | Value for NACA 0020 Airfoil/mm |
|---|---|
| *L* | 480 |
| *Lc* | 6.0 |
| *La* | 6.0–12.0 |
| *Lb* | 3.0–4.2 |
| *Lh* | 1.0 |

## 3. Numerical Analysis and Methodology

### *3.1. Numerical Scheme and Boundary Conditions*

Methane was modeled as a turbulent flow in three-dimensional space, with density varying significantly with temperature while being approximately incompressible under pressure variations. The operating pressure was maintained constant at 8 MPa, above the critical pressure (4.6 MPa). The inlet temperature was set at 110 K, below the critical temperature of 190.6 K, while the outlet temperature exceeded this critical value. Consequently, the fluid undergoes a transcritical heating process, transitioning from a subcritical to a supercritical state. Within the computational domain, a gravitational acceleration of 9.8 m·s$^{-2}$ was applied along the negative y-axis. As illustrated in Figure 2, Symmetry boundary conditions were

applied to the lateral walls of the airfoil-fin PCHE channels, and periodic boundary conditions were imposed on the top and bottom walls, which allows a reduction in the computational domain [28]. The fluid and solid domains were thermally coupled via conjugate heat transfer at the contacting interfaces. A mass-flow inlet and a pressure-outlet boundary condition were applied, with 20 mm-long extensions incorporated at both the inlet and outlet sections. The operating conditions are specified in Table 2.

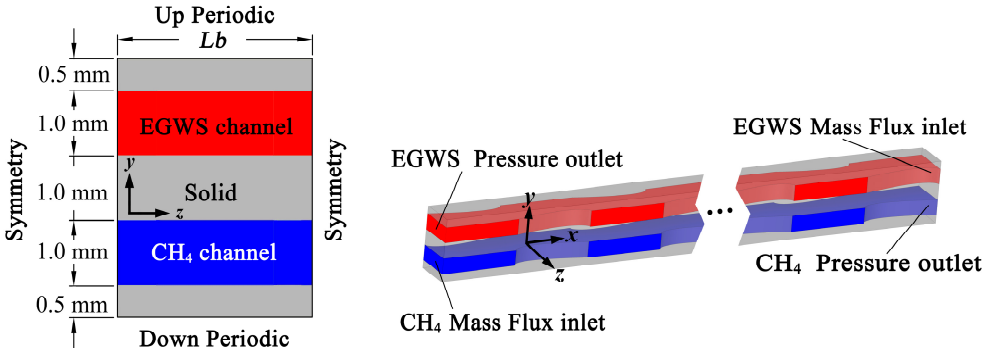



**Figure 2.** Boundary conditions of the numerical model.

**Table 2.** Operating conditions of the numerical model.

| Parameters | Cold Channel ($CH_4$) | | Hot Channel (EGWS) | |
|---|---|---|---|---|
| | Inlet | Outlet | Inlet | Outlet |
| $T$/K | 110 | — | 343.15 | — |
| $P$/MPa | — | 8.00 | — | 0.40 |
| $G$/kg·m$^{-2}$·s$^{-1}$ | 100–300 | — | 250–1500 | — |

The thermal radiation effect is neglected as its magnitude is orders of magnitude smaller than that of forced convection. A pressure-based, implicit double-precision solver employing the SST $k$-$\omega$ [9,29,30] with enhanced wall treatment turbulence model was used for the numerical simulations. Pressure-velocity coupling was handled with the SIMPLEC algorithm, and the convective terms in both the momentum and energy equations were discretized using the second-order upwind scheme. Convergence was ensured with residuals below $10^{-5}$ for all variables and below $10^{-8}$ for the energy equation.

### *3.2. Transcritical Methane Properties*

The pronounced variations in the thermophysical properties of transcritical $CH_4$, particularly near the pseudo-critical region, necessitated the use of user-defined functions (UDFs) to accurately incorporate these changes into our analysis (see UDF files in the Supplementary Material). To achieve this, the thermophysical properties of methane from 100 K to 380 K at 8 MPa were calculated using NIST REFPROP 9.1 [31], as shown in Figure 3. These properties were then fitted into piecewise polynomial functions of temperature using Origin 2024b, achieving an $R^2$ of 0.99 with a maximum error of less than 1%, as presented in Table 3. This methodology ensures that the unique thermophysical behavior of transcritical $CH_4$ is adequately represented, enabling more precise modeling and predictions under the specified operating conditions.

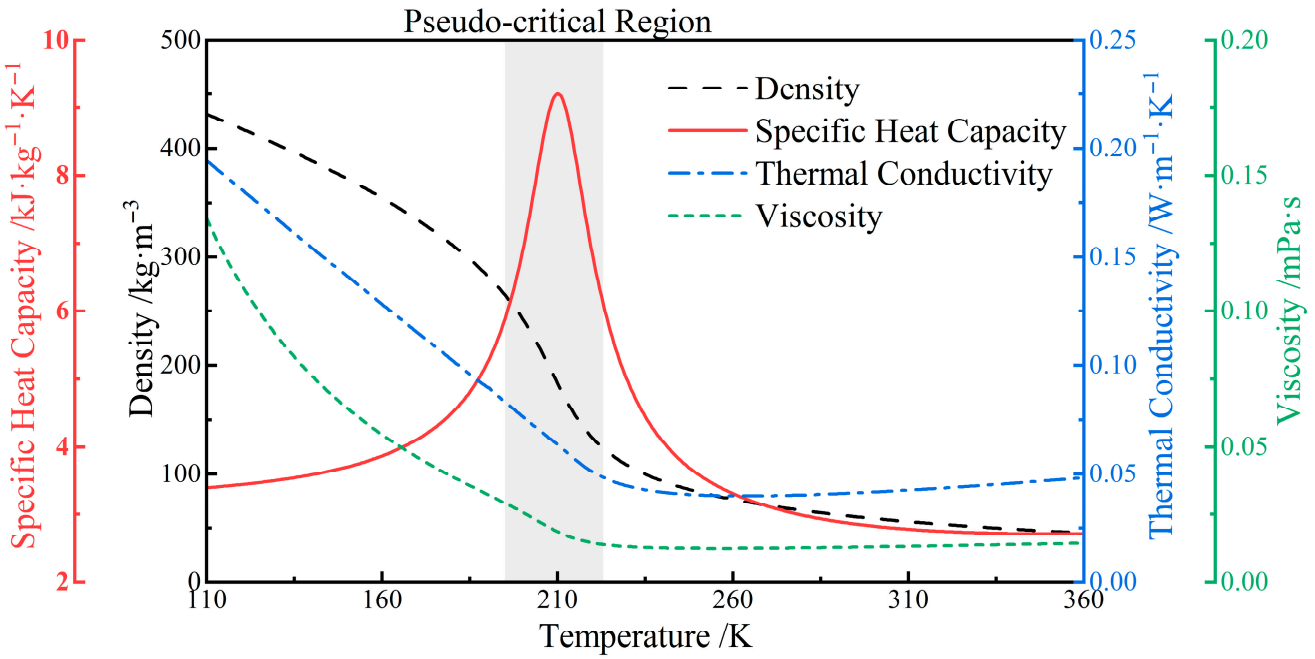



**Figure 3.** Fluctuations in $CH_4$ properties in the pseudo-critical region at an operating pressure of 8 MPa.

**Table 3.** Property correlations of $CH_4$ at 8 MPa.

| | *T*/K | Value |
|---|---|---|
| $C_p$/ J·kg$^{-1}$·K$^{-1}$ | 100.00–201.07 | $-139{,}471 + 5294.940\,T - 77.874081\,T^2 + 0.568005416\,T^3 - 0.002055837992\,T^4 + 2.96123118 \times 10^{-6}\,T^5$ |
| | 201.07–230.10 | $2{,}002{,}157{,}650 - 46{,}541{,}536.180\,T + 432{,}313.583830\,T^2 - 2005.807821461\,T^3 + 4.648594724190\,T^4 - 4.305237019249 \times 10^{-3}\,T^5$ |
| | 230.10–380.00 | $894{,}845 - 13{,}892.327\,T + 86.614360\,T^2 - 0.269923026\,T^3 + 4.2004972 \times 10^{-4}\,T^4 - 2.6093962 \times 10^{-7}\,T^5$ |
| $\rho$/ kg·m$^{-3}$ | 100.00–199.74 | $-7.36 + 16.05319\,T - 0.193898572\,T^2 + 9.6630367 \times 10^{-4}\,T^3 - 1.83305 \times 10^{-6}\,T^4$ |
| | 199.74–230.69 | $-610{,}201.80 + 11{,}309.91144\,T - 78.36465942\,T^2 + 0.240730569\,T^3 - 2.7674608 \times 10^{-4}\,T^4$ |
| | 230.69–380.00 | $3338.65 - 38.78081\,T + 0.17407336\,T^2 - 3.5046538 \times 10^{-4}\,T^3 + 2.6546299 \times 10^{-7}\,T^4$ |
| $\lambda$/ W·m$^{-1}$·K$^{-1}$ | 100.00–212.44 | $0.2248 + 0.0018988\,T - 3.30252 \times 10^{-5}\,T^2 + 1.464454 \times 10^{-7}\,T^3 - 2.364564 \times 10^{-10}\,T^4$ |
| | 212.44–237.27 | $-87.8483 + 1.6063521\,T - 0.0109614669\,T^2 + 3.3122684465 \times 10^{-5}\,T^3 - 3.74177905 \times 10^{-8}\,T^4$ |
| | 237.27–380.00 | $0.8911 - 0.0104169\,T + 4.72869 \times 10^{-5}\,T^2 - 9.48681 \times 10^{-8}\,T^3 + 7.17469 \times 10^{-11}\,T^4$ |
| $\mu$/ Pa·s | 100.00–161.19 | $0.00275132 - 6.670457 \times 10^{-5}\,T + 6.5116435 \times 10^{-7}\,T^2 - 2.92435980 \times 10^{-9}\,T^3 + 5.01159500 \times 10^{-12}\,T^4$ |
| | 161.19–223.04 | $0.00622501 - 1.2949471 \times 10^{-4}\,T + 1.02437810 \times 10^{-6}\,T^2 - 3.61382924 \times 10^{-9}\,T^3 + 4.77175361 \times 10^{-12}\,T^4$ |
| | 223.04–380.00 | $2.67271608 \times 10^{-4} - 3.21883 \times 10^{-6}\,T + 1.507953 \times 10^{-8}\,T^2 - 3.113266 \times 10^{-11}\,T^3 + 2.405444 \times 10^{-14}\,T^4$ |

### *3.3. Governing Equations and Turbulence Model*

$CH_4$ and EGWS were selected as the working fluid, with the following governing equations.

Continuity equation:

$$\frac{\partial \rho}{\partial t} + \nabla\left(\rho \vec{V}\right) = 0 \tag{4}$$

Momentum conservation equation:

$$\frac{\partial\left(\rho u_i u_j\right)}{\partial x_i} = -\frac{\partial p}{\partial x_i} + \frac{\partial}{\partial x_j}\left[\left(\mu_t + \mu\right) - \left(\frac{\partial u_i}{\partial x_j} + \frac{\partial u_j}{\partial x_i}\right) - \frac{2}{3}\left(\mu_t + \mu\right)\frac{\partial u_i}{\partial x_i}\delta_{ij}\right] \tag{5}$$

Energy conservation equation:

$$\frac{\partial\left(\rho u_i C_p T\right)}{\partial x_i} = \frac{\partial}{\partial x_i}\left(\lambda \frac{\partial T}{\partial x_j}\right) + \Phi \tag{6}$$

The SST $k$-$\omega$ turbulence model incorporates the benefits of both the standard $k$-$\varepsilon$ and $k$-$\omega$ models, enabling precise prediction of flow separation in response to adverse pressure gradients [24]. The governing equations are presented below:

$$\frac{\partial(\rho k)}{\partial t} + \frac{\partial\left(\rho u_j k\right)}{\partial x_j} = p - \beta^* \omega k + \frac{\partial}{\partial x_j}\left[\left(\mu + \sigma_k \mu_t\right)\frac{\partial k}{\partial x_j}\right] \tag{7}$$

$$\frac{\partial(\rho\omega)}{\partial t} + \frac{\partial\left(\rho u_j \omega\right)}{\partial x_j} = \frac{\gamma\rho}{\mu_t} p - \beta\rho\omega^2 + \frac{\partial}{\partial x_j}\left[\left(\mu + \sigma_k \mu_t\right)\frac{\partial k}{\partial x_j}\right] + 2(1 - F_1)\frac{\rho\sigma_\omega}{\omega}\frac{\partial k}{\partial x_j}\frac{\partial \omega}{\partial x_j} \tag{8}$$

### *3.4. Definition of Performance Parameters*

To facilitate the discussion of simulation results for the PCHE, the key parameters used in this study are defined as follows:

Hydraulic diameter ($D_h$/mm):

The hydraulic diameter [7] is calculated using Equation (9), with the relevant parameters illustrated in Figures 1d and 4.

$$\begin{aligned} V &= Lh(Lb \cdot Ln - 2Sa) \\ S &= 2[Lh(Ld + La) + Lb \cdot Ln - 2Sa] \\ D_h &= \tfrac{4V}{S} \end{aligned} \tag{9}$$

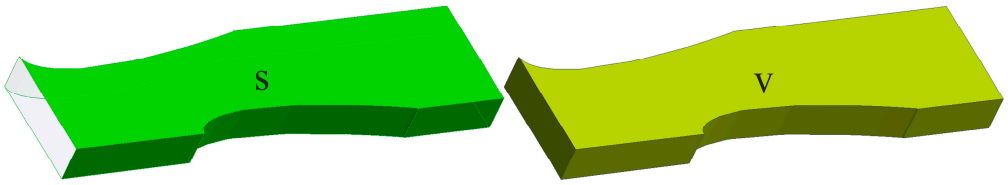



**Figure 4.** Calculation Principle of $D_h$ based on Wetted Surface Area ($S$) and Flow Volume ($V$).

Convective heat transfer coefficient ($h$/kW·m$^{-2}$·K$^{-1}$), Reynolds number ($Re$), and Prandtl number ($Pr$):

$$h = \frac{q}{(T_W - T_b)} \tag{10}$$

$$Re = \frac{\rho u D_h}{\mu} \tag{11}$$

$$Pr = \frac{C_p \mu}{\lambda} \tag{12}$$

Nusselt number ($Nu$), Fanning friction factor ($f_{\text{Fanning}}$):

$$Nu = \frac{hD_{\text{h}}}{\lambda} \tag{13}$$

$$f_{\text{Fanning}} = \frac{\Delta p_f D_{\text{h}}}{2\rho L \bar{u}^2} \tag{14}$$

$$\Delta p_f = \Delta p - \Delta p_a = \Delta p - \left(\rho_{\text{out}} u_{\text{out}}^2 - \rho_{\text{in}} u_{\text{in}}^2\right) \tag{15}$$

For the screening and optimization of structures, the Thermal Performance Factor ($TPF$) [26] is employed to quantitatively assess the thermal-hydraulic performance of PCHEs. It is defined as:

$$TPF = \frac{Nu/Nu_0}{\left(f_{\text{Fanning}}/f_{\text{Fanning0}}\right)^{\frac{1}{3}}} \tag{16}$$

This factor is calculated under the same mass flow rate condition. Based on its definition, TPF directly represents the relative convective heat transfer capability of different geometric structures under the same flow pressure drop. A $TPF > 1$ indicates that the structure can achieve stronger heat transfer without increasing the system pumping cost, which aligns with the established performance evaluation philosophy for enhanced heat transfer surfaces under fixed pumping power constraints [32].Under transcritical conditions with drastic thermophysical property variations, the traditional fin efficiency analysis based on constant properties becomes inadequate, as such analyses require modification under variable-property conditions [33]. The $TPF$ adopted in this study, as an integrated thermal-hydraulic performance metric, thus provides a more direct and practical criterion for assessing the effectiveness of PCHE channels as extended surfaces under these complex operating conditions. The values of $Nu_0$ and $f_{\text{Fanning0}}$ presented in this study are calculated for the condition of $Ks$ = 1.0, $Kb$ = 0.5, and $Ka$ = 1.0.

Root mean square deviation ($E_{\text{RMS}}$):

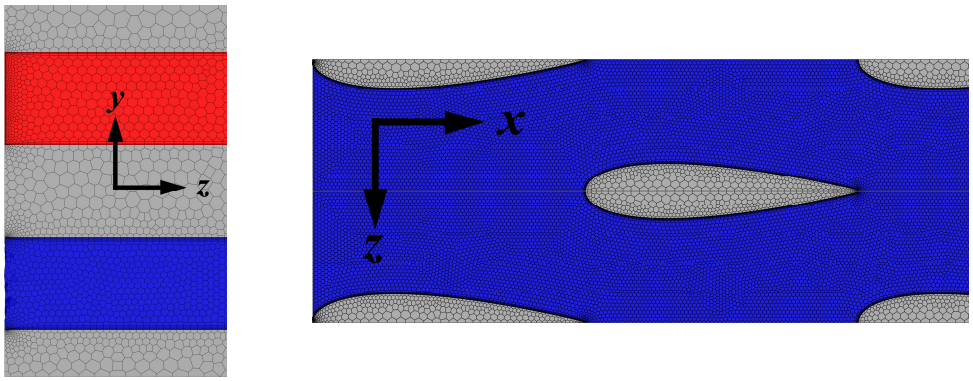
$$E_{\text{RMS}} = \sqrt{\frac{\sum_{i=1}^{n}\left(\frac{X_{\text{num}} - X_{\text{pred}}}{X_{\text{num}}}\right)^2}{n}} \times 100\% \tag{17}$$

### *3.5. Mesh Generation and Grid Independence Verification*

#### 3.5.1. Mesh Generation

Mesh generation constitutes a critical preprocessing step that directly affects both the accuracy and computational efficiency of numerical simulations. The 3D computational model was developed using ANSYS 2022R1 DesignModeler, and mesh generation was performed in ANSYS 2022R1 Fluent Meshing.

As illustrated in Figure 5, boundary layers were applied to the fluid domain at the fluid-solid interfaces to meet the computational accuracy requirements of the SST $k$-$\omega$ turbulence model, with a first-layer height of 0.01 mm and a growth rate of 1.2. This ensures $y^+ \leq 1$ under all simulated conditions, allowing direct resolution of the viscous sublayer. Enhanced wall treatment was adopted in the simulations.




(**a**) (**b**)

**Figure 5.** Mesh generation: (**a**) mesh of cross-section, and (**b**) mesh of airfoil fins.

#### 3.5.2. Grid Independence Verification

Grid independence is considered achieved when localized refinement of the computational mesh no longer significantly affects the simulation results. In this study, six mesh configurations with progressively increasing resolution were generated for the single-airfoil channel model, containing 5.55, 6.14, 7.16, 8.13, 9.72, and 11.6 million cells, respectively. Under identical boundary conditions, calculations were conducted for all six mesh configurations. As illustrated in Figure 6, when the mesh count exceeds 8.13 million cells, further refinement results in variations of less than 1% in both outlet temperature difference and pressure drop due to grid discretization. Considering the balance between computational accuracy and efficiency, the airfoil channel model with 8.13 million grid cells was adopted for all subsequent analyses.

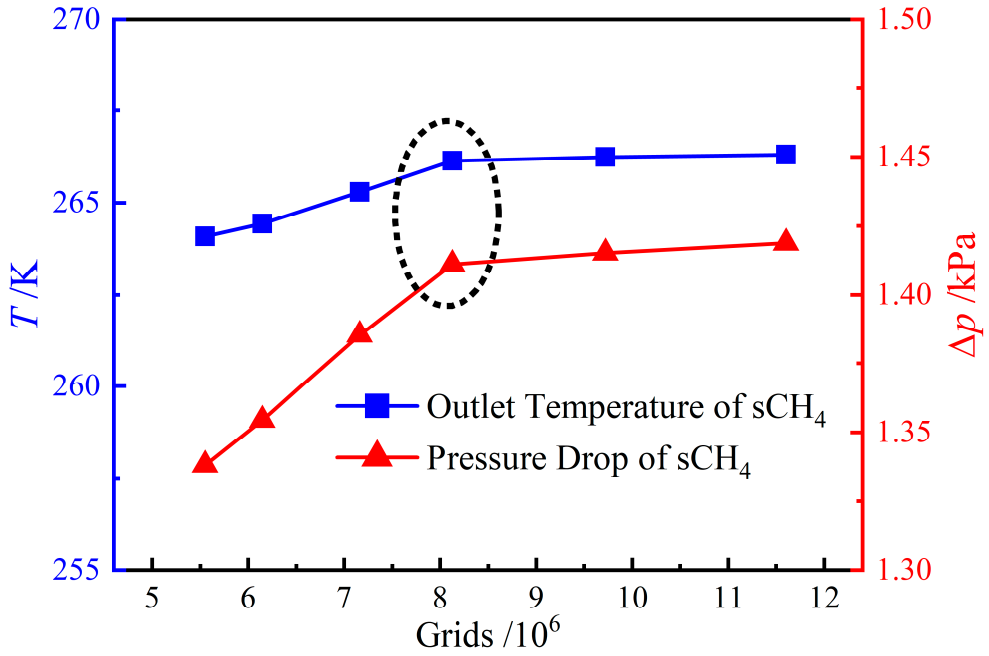



**Figure 6.** Verification of grid independence.

### *3.6. Model Validation*

To ensure the accuracy of the numerical model and simulation methodology, this study was benchmarked against the experimental investigations and validated numerical simulation results reported by Zhao et al. [34]. Adopting the same numerical approach employed in their work, the comparative analysis demonstrates good agreement between

the computational results, with a maximum deviation of 5% in the convective heat transfer coefficient ($h$) and 8% in the extended pressure drop, as illustrated in Figure 7. The strong consistency validates the accuracy of the numerical model and computational methodology adopted in this study.

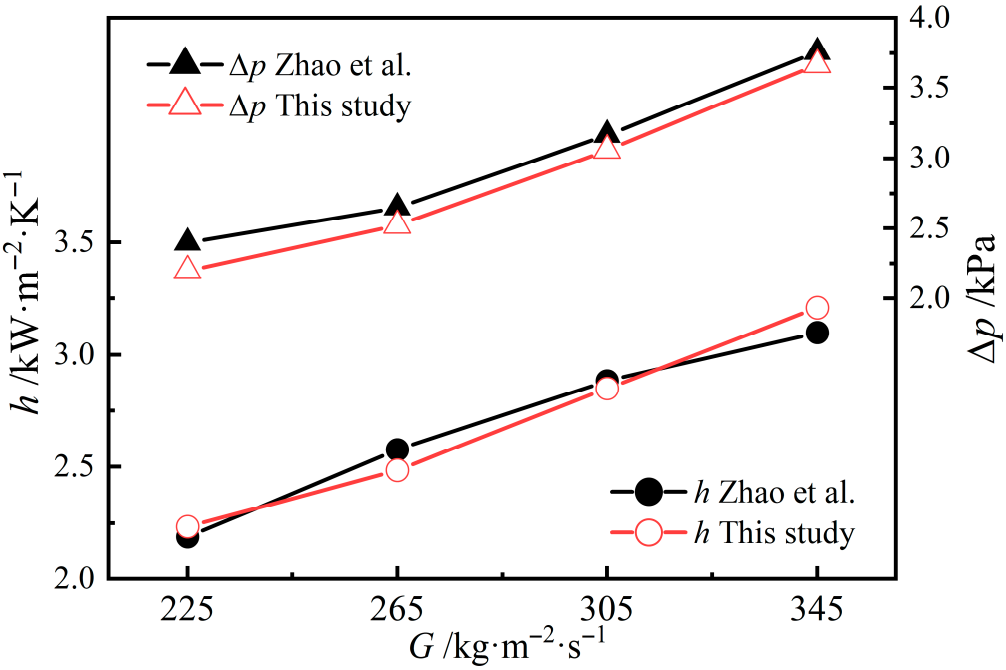


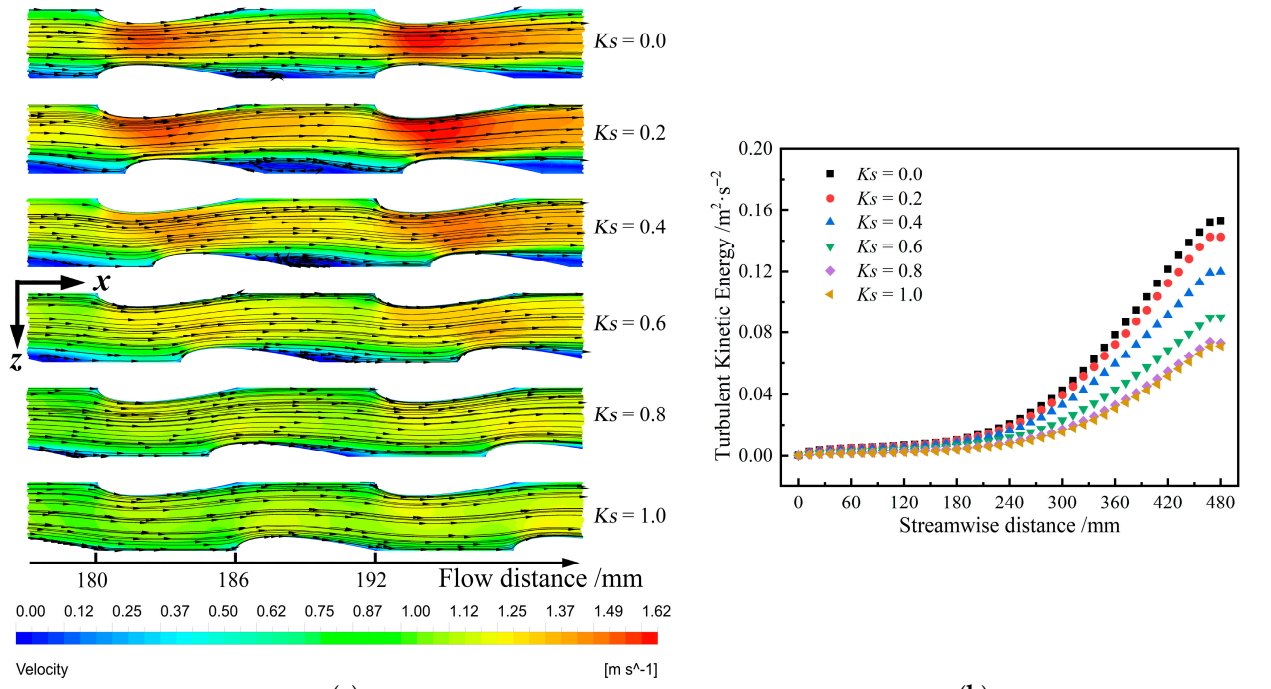

**Figure 7.** Validation of the numerical results with experimental heat transfer coefficient for different mass flux ($G$) values [34].

## 4. Results and Discussion

### *4.1. Effect of Airfoil Fin Array Longitudinal Staggering Ratio (Ks)*

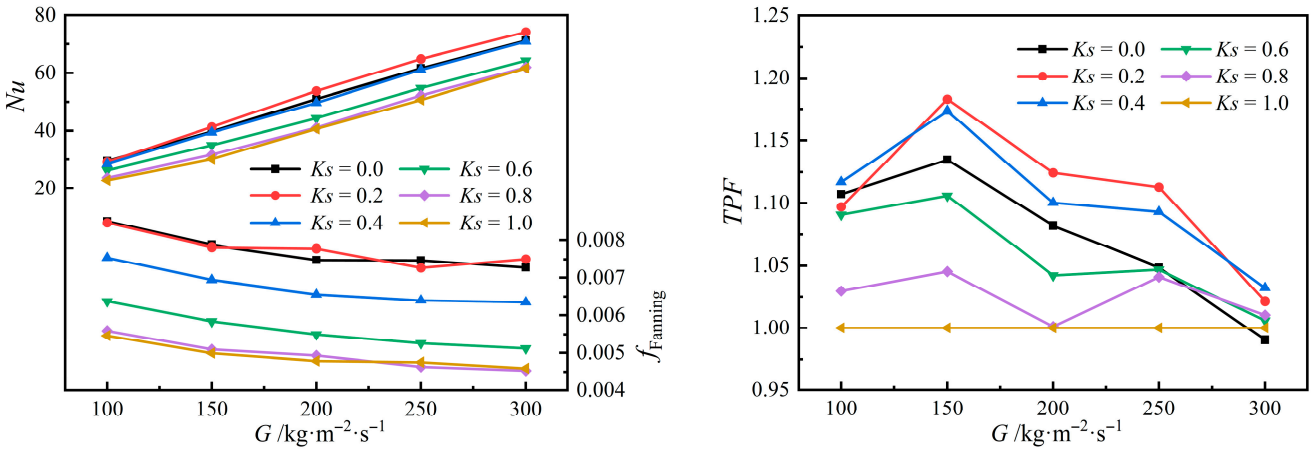
Figure 8 presents the influence of different $Ks$ on the velocity streamline distribution near the quasi-critical region, under the conditions of $Ka$ = 1.0, $Kb$ = 0.5, and $G$ = 200 kg·m$^{-2}$·s$^{-1}$. Within the range $Ks$ = 0, 0.2, and 0.4, the fluid demonstrates contraction and expansion behavior between fins, with frequent changes in flow direction. This behavior induces pronounced separation and reattachment phenomena dominated by pressure gradients and inertial forces. Periodically shed turbulent vortex structures, such as Karman and horseshoe vortices, are observed at the fin trailing edges and within the gap region. These vortical structures enhance fluid mixing and disrupt the thermal boundary layer, thereby intensifying the heat transfer process. Conversely, under conditions of $Ks$ = 0.8 and 1.0, the streamline distribution becomes more uniform, and the turbulent vortex structures are markedly weakened.

Figure 9a presents the influence of $Ks$ on thermohydraulic performance. When $Ks$ = 0.0, 0.2, and 0.4, the $CH_4$ exhibits higher turbulence intensity within the airfoil-shaped channel compared to the cases of $Ks$ = 0.6, 0.8, and 1.0. Specifically, at $Ks$ = 0.2, the moderate spacing between front and rear fins increases turbulence mixing while increasing flow velocity, leading to a higher $Nu$ than other configurations and achieving optimal heat transfer performance. However, the corresponding $f_{\text{Fanning}}$ is also higher, indicating increased flow resistance. In contrast, when $Ks$ = 0.6, 0.8, and 1.0, flow within the channel becomes smoother, and turbulence intensity decreases. The increased fin spacing enlarges the flow area, leading to reduced flow velocity and turbulence levels, which lowers the $Nu$ while simultaneously decreasing the $f_{\text{Fanning}}$.




(**a**) (**b**)

**Figure 8.** Flow field and turbulence characteristics of $sCH_4$ near the pseudo-critical zone for various longitudinal staggering ratio (*Ks*) values at the operating conditions of *Ka* = 1.0, *Kb* = 0.5, and $G = 200\ kg{\cdot}m^{-2}{\cdot}s^{-1}$. (**a**) Velocity contour with streamlines on the central x-z cross-section, and (**b**) Turbulent kinetic energy along the flow direction.




(**a**) (**b**)

**Figure 9.** Thermal-hydraulic performance versus mass flux *G* for various *Ks* values at the operating conditions of *Ka* = 1.0 and *Kb* = 0.5. (**a**) Nusselt number (*Nu*) and Fanning friction factor ($f_{Fanning}$), and (**b**) thermal performance factor (*TPF*, baseline: *Ks* = 1.0, *Kb* = 0.5, *Ka* = 1.0).

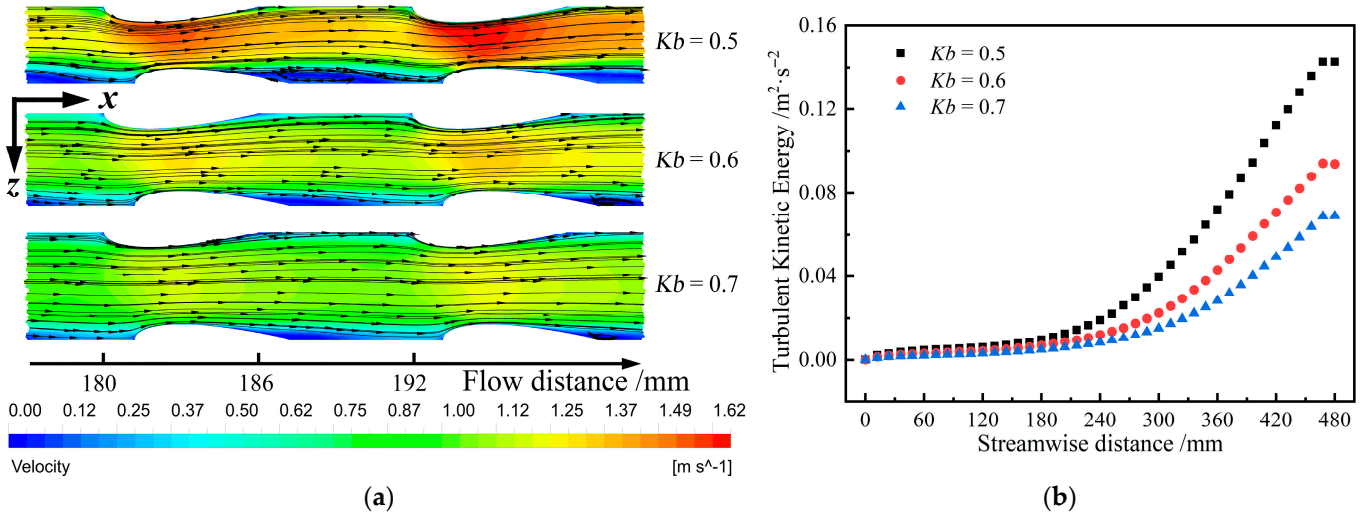
Figure 9b further illustrates that the *TPF* initially increases and then decreases with mass flux (*G*). Near the common engineering mass flux of $G = 200\ kg{\cdot}m^{-2}{\cdot}s^{-1}$, the *TPF* for the *Ks* = 0.2 configuration is significantly higher than those of other configurations. Considering both heat transfer performance and pressure drop characteristics, the airfoil channel with *Ks* = 0.2 demonstrates optimal performance, achieving a *TPF* up to 1.18 times higher than that of the fully staggered longitudinal structure (*Ks* = 1.0).

Notably, low-velocity recirculation zones persist near the wall corners and in the backflow regions of the airfoil fins due to flow separation. In these areas, fluid renewal

is slow, where heat transfer is dominated by conduction with minimal convective effects. These conditions result in increased local thermal resistance and reduced heat transfer efficiency. Consequently, the flow within the airfoil fin channel exhibits dual characteristics: enhanced heat transfer due to turbulent vortex structures, along with reduced effective heat transfer area and increased flow resistance caused by stagnant zones.

### *4.2. Effect of Airfoil Fin Array Transverse Pitch Ratio (Kb)*

Figure 10 illustrates the velocity and streamline distributions near the quasi-critical region under the conditions $Ks$ = 0.2, $Ka$ = 1.0, and $G$ = 200 kg·m$^{-2}$·s$^{-1}$ for various lateral spacing parameters ($Kb$ = 0.5, 0.6, 0.7). It is observed that as the lateral spacing decreases, the flow cross-section contracts significantly, resulting in a more pronounced acceleration effect between adjacent fins. This leads to a substantial increase in local flow velocity under the same inlet mass flux. Simultaneously, the reduced lateral spacing intensifies fluid shear forces, promoting stronger flow separation at the fin trailing edges and near-wall regions. This produces smaller-scale, higher-intensity turbulent vortex structures, such as more distinct and densely distributed Karman vortices and separation vortices. These vortex structures are transported downstream with the main flow, increasing mixing and heat exchange between fluid particles.




(**a**) (**b**)

**Figure 10.** Flow field and turbulence characteristics of $CH_4$ near the pseudo-critical zone for various airfoil fin array transverse pitch ratio ($Kb$) values under the operating conditions of $Ks$ = 0.2, $Ka$ = 1.0, and $G$ = 200 kg·m$^{-2}$·s$^{-1}$. (**a**) Velocity contour with streamlines on the central x-z cross-section, and (**b**) Turbulent kinetic energy along the flow direction.

Figure 11 presents velocity and streamline distributions on three characteristic cross-sections perpendicular to the flow, obtained near the quasi-critical region for three different lateral spacings ($Kb$ = 0.5, 0.6, 0.7). Complex secondary flow structures, induced by longitudinal fin misalignment, were observed under all operating conditions. When $Kb$ = 0.5, cross-sectional flow lines revealed pronounced vortex structures, including horseshoe vortices and corner vortices visible near the leading and trailing fin edges. These vortex structures substantially enhanced fluid mixing and increased local velocity gradients. As $Kb$ increases to 0.6, the vortex scale grows while intensity slightly decreases, yet the flow field inhomogeneity remains significant. At $Kb$ = 0.7, the flow line distribution across the cross-section becomes smoother, with reduced secondary flow intensity and a more uniform velocity distribution, indicating minimal disturbance of the flow field by fins at larger spacings.

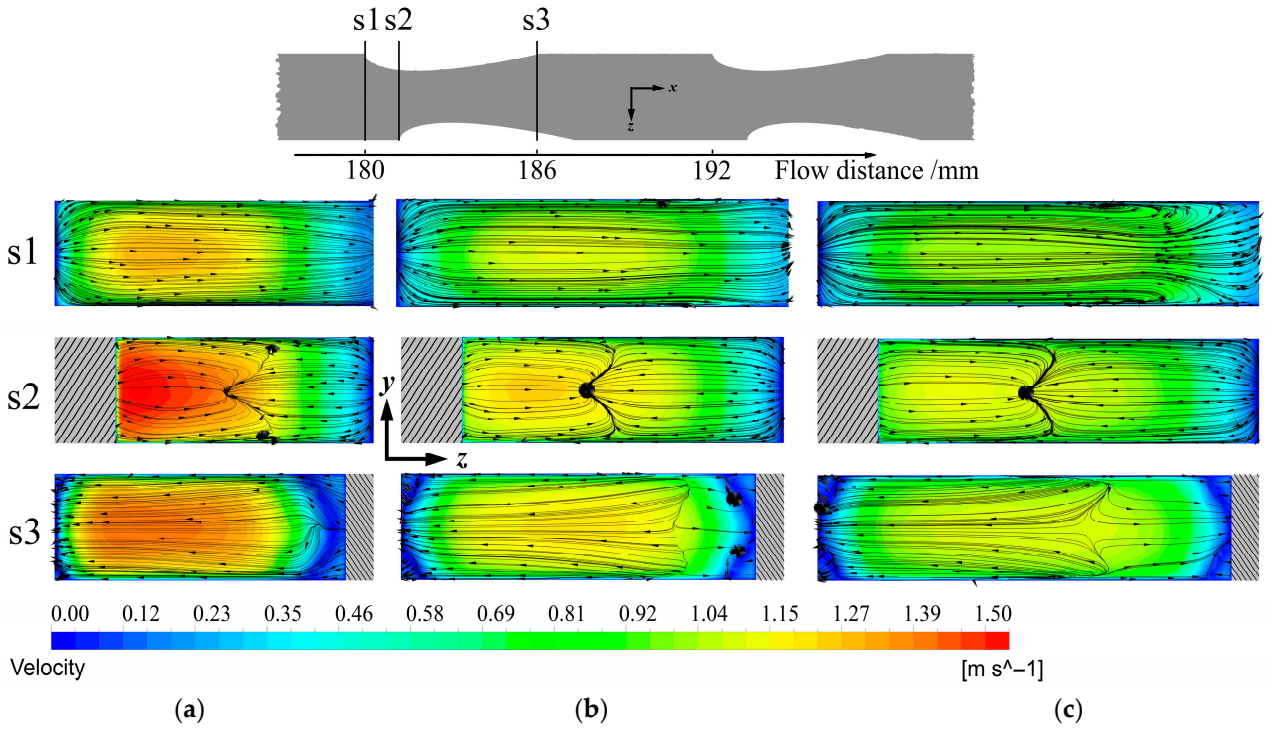



**Figure 11.** Velocity and streamline fields at different axial locations near $CH_4$ pseudo-critical zone for *Kb* values at the operating conditions of *Ks* = 0.2 and *Ka* = 1.0. (**a**) *Kb* = 0.5; (**b**) *Kb* = 0.6; (**c**) *Kb* = 0.7.

Comparing flow structures at various axial positions under the same lateral spacing (s1: leading edge of the first fin, s2: leading edge of the second staggered fin, s3: trailing edge region of the first fin) indicates that high-velocity zones and intense vortices generally develop at fin initiation regions (s1, s2) owing to flow impact and abrupt directional changes. Conversely, the trailing edge region (s3) typically exhibits low-velocity recirculation and vortex shedding, a phenomenon particularly pronounced at smaller lateral spacings. Reduced lateral spacings readily induce high-intensity secondary flows and turbulent mixing but result in higher flow energy consumption; increasing the spacing diminishes flow resistance while weakening heat transfer enhancement.

Figure 12a presents the variation in *Nu* and $f_{\text{Fanning}}$ with lateral fin spacing. It is observed that as the lateral spacing decreases, *Nu* increases markedly. This is primarily attributed to the intensified flow channel contraction effect, elevated fluid velocity, increased turbulence intensity, and reduced thermal boundary layer thickness, all of which enhance the convective heat transfer process. However, the small spacing also amplifies flow separation and shear effects, leading to higher flow resistance, manifested as a significant rise in the $f_{\text{Fanning}}$.

Figure 12b depicts the trend of the *TPF* as a function of *G* for different lateral spacings. With increasing *G*, the *TPF* for all three spacing configurations initially increases and then decreases. At the commonly encountered engineering mass flux of $G = 200\ \text{kg}\cdot\text{m}^{-2}\cdot\text{s}^{-1}$, the *TPF* value reaches its peak for the lateral spacing parameter *Kb* = 0.5. This optimal value arises because, up to this critical spacing, the enhanced fluid mixing significantly improves heat transfer, an effect that outweighs the associated pressure drop penalty. This indicates that under these operating conditions, the *Kb* = 0.5 configuration achieves an optimal balance between enhanced heat transfer and controlled pressure drop, demonstrating superior overall thermal-hydraulic performance.

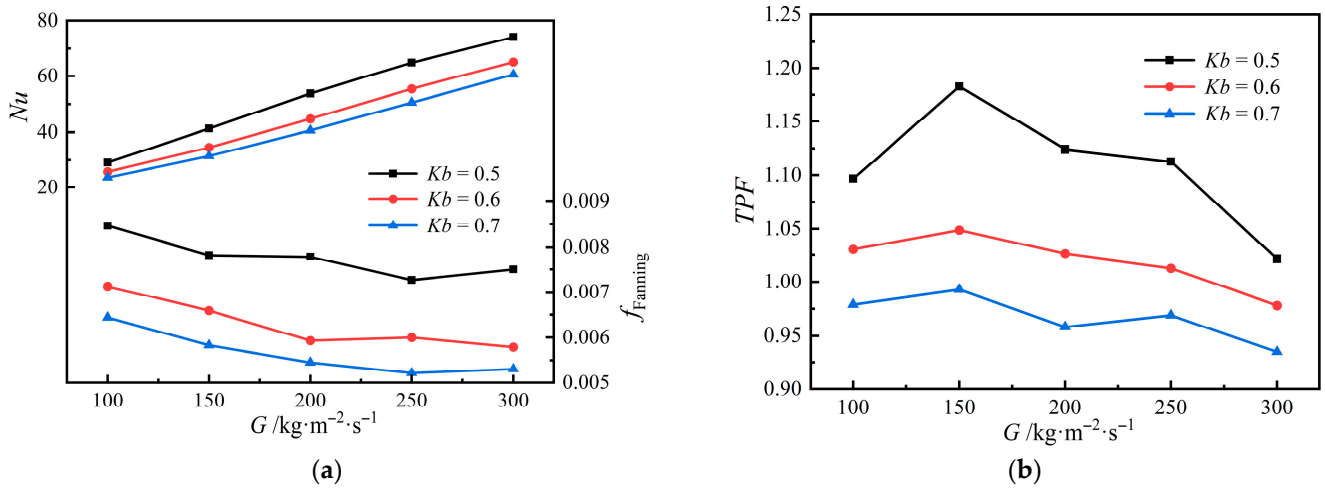



**Figure 12.** Thermal-hydraulic performance versus mass flux *G* for various *Kb* values at the operating conditions of *Ks* = 0.2 and *Ka* = 1.0. (**a**) *Nu* and $f_{\text{Fanning}}$, and (**b**) *TPF* (baseline: *Ks* = 1.0, *Kb* = 0.5, *Ka* = 1.0).

### *4.3. Effect of Airfoil Fin Array Longitudinal Pitch Ratio (Ka)*

Figure 13 illustrates the velocity distribution and streamlines near the quasi-critical region for various longitudinal spacing coefficients (*Ka* = 1.0, 1.5, 2.0) under the conditions of *Ks* = 0.2, *Kb* = 0.5, and *G* = 200 kg·m$^{-2}$·s$^{-1}$. When *Ka* = 1.0, a pronounced channel constriction effect occurs, leading to notable fluid acceleration. High-intensity and high-frequency turbulent vortex shedding appears near the trailing edge of the fins. The secondary flow structures are complex, exhibiting significant streamline curvature. These vigorous vortex formations effectively disrupt the thermal boundary layer, enhance fluid mixing, and thereby improve heat transfer. However, this also results in an accompanying increase in flow resistance. As *Ka* increases to 1.5, the flow disturbance between fins weakens, velocity distribution becomes more uniform, vortex intensity and scale decrease, and streamline curvature is moderated. This behavior indicates a reduction in both heat transfer enhancement and flow resistance. At *Ka* = 2.0, the flow disturbance between fins is minimal, the flow field becomes smoother and more uniform, and turbulence intensity is markedly reduced.

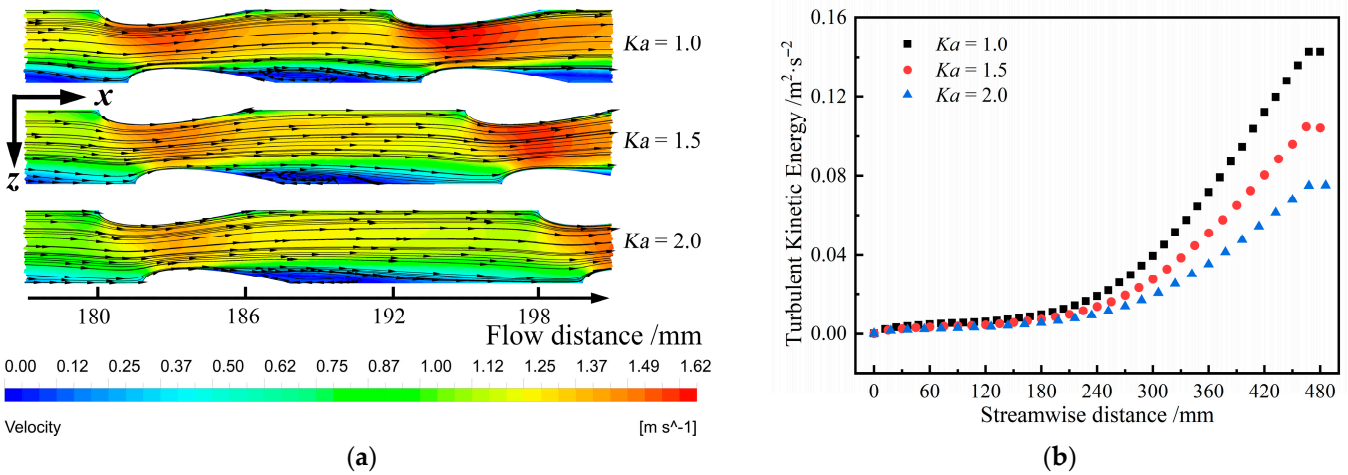



**Figure 13.** Flow field and turbulence characteristics of $CH_4$ near the pseudo-critical zone for various airfoil fin array longitudinal pitch ratio (*Ka*) values at the operating conditions of *Ks* = 0.2, *Kb* = 0.5, and *G* = 200 kg·m$^{-2}$·s$^{-1}$. (**a**) Velocity contour with streamlines on the central x-z cross-section, and (**b**) turbulent kinetic energy along the flow direction.

Figure 14a illustrates the variation in $Nu$ and $f_{\text{Fanning}}$ with $Ka$ at different $G$. Under identical operating conditions, $Nu$ attains its maximum at $Ka$ = 1.0, exhibiting an approximately 13% increase compared to $Ka$ = 2.0. This result indicates that the intensified turbulent disturbances caused by the smaller longitudinal spacing are the primary mechanism for heat transfer enhancement. Simultaneously, $f_{\text{Fanning}}$ at $Ka$ = 1.0 increases by ~22% relative to $Ka$ = 2.0, indicating that the performance improvement is accompanied by a significant rise in pump power consumption.

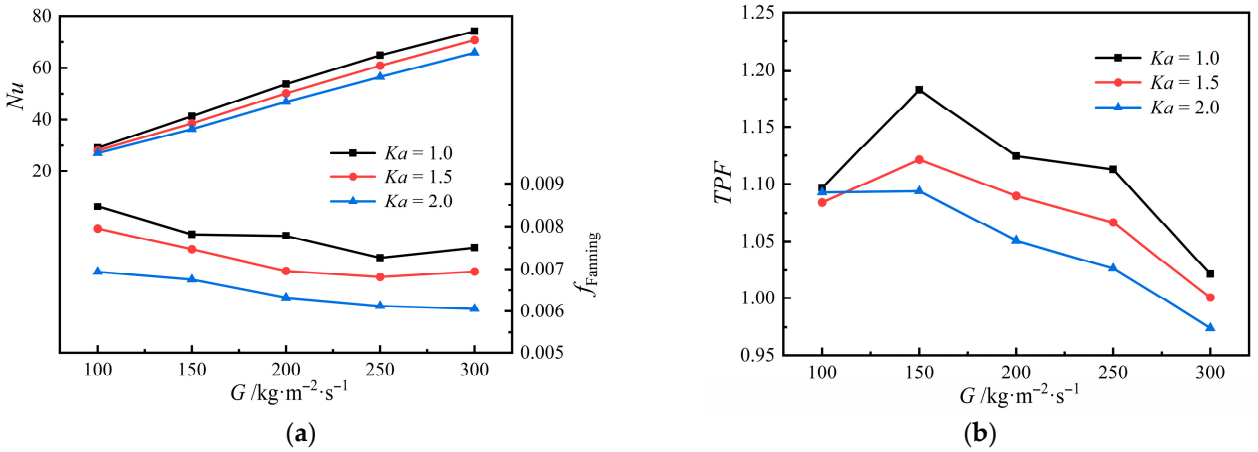



**Figure 14.** Thermal-hydraulic performance versus mass flux $G$ for various $Ka$ values under the operating conditions of $Ks$ = 0.2 and $Kb$ = 0.5. (**a**) $Nu$ and $f_{\text{Fanning}}$, and (**b**) $TPF$ (baseline: $Ks$ = 1.0, $Kb$ = 0.5, $Ka$ = 1.0).

Figure 14b presents the variation in $TPF$ with $G$. Around the typical engineering mass flux of $G$ = 200 kg·m$^{-2}$·s$^{-1}$, the $TPF$ initially increases and then decreases as $G$ increases. The maximum $TPF$ is obtained at $Ka$ = 1.0, where the overall thermal-hydraulic performance is optimal, exhibiting a significant improvement over the baseline case of $Ka$ = 2.0 (refer to the figure for specific values). Although the configuration with $Ka$ = 1.5 provides a partial balance between heat transfer enhancement and flow resistance, its $TPF$ remains lower than that of the $Ka$ = 1.0 structure. These findings indicate that, within the investigated parameter range, the $Ka$ = 1.0 configuration achieves a marked enhancement in heat transfer performance with an acceptable pressure drop cost, demonstrating superior engineering applicability.

### *4.4. Heat Transfer Performance Prediction*

The preceding analysis indicates that mass flux (closely related to $Re$), airfoil fin array longitudinal staggering ratio ($Ks$), airfoil fin array transverse pitch ratio ($Kb$), and airfoil fin array longitudinal pitch ratio ($Ka$) are key parameters governing the overall performance of the PCHE. Based on the numerical simulation results, dimensionless correlations were developed to predict $Nu$ and $f_{\text{Fanning}}$. Consequently, dimensionless correlations were established to predict the flow and heat transfer characteristics of transcritical $CH_4$ within PCHE channels.

$$Nu = 0.0002Re^{1.28}Pr^{-2.12}Kb^{-0.17}Ka^{-0.0086}\left(3.96 - |0.11 - Ks|^{0.41}\right)^{-0.77} \quad (18)$$

$$f_{\text{Fanning}} = 0.00108Re^{0.166}Pr^{-2.56}Kb^{-0.28}Ka^{-0.12}\left(2.73 - |0.88 - Ks|^{0.55}\right)^{-1.37} \quad (19)$$

The correlation exhibits good applicability within the following parameter ranges: $Lc$ = 6 mm, $Ks$ = 0.0–1.0, $Kb$ = 0.5–0.7, $Ka$ = 1.0–2.0, $Re$ = 8000–25,000, and $Pr$ = 1.53–1.86.

A comparison between the numerical results and the predictions obtained from the proposed correlation is shown in Figure 15, with deviations confined within ±10%. The correlation exhibits good applicability within the following parameter ranges: $Lc$ = 6 mm, $Ks$ = 0.0–1.0, $Kb$ = 0.5–0.7, $Ka$ = 1.0–2.0, $Re$ = 8000–25,000, and $Pr$ = 1.53–1.86. The deviations calculated using Equation (17) for $Nu$ and $f_{\text{Fanning}}$ are 2.08% and 6.57%, respectively, demonstrating the high accuracy of the developed correlation.

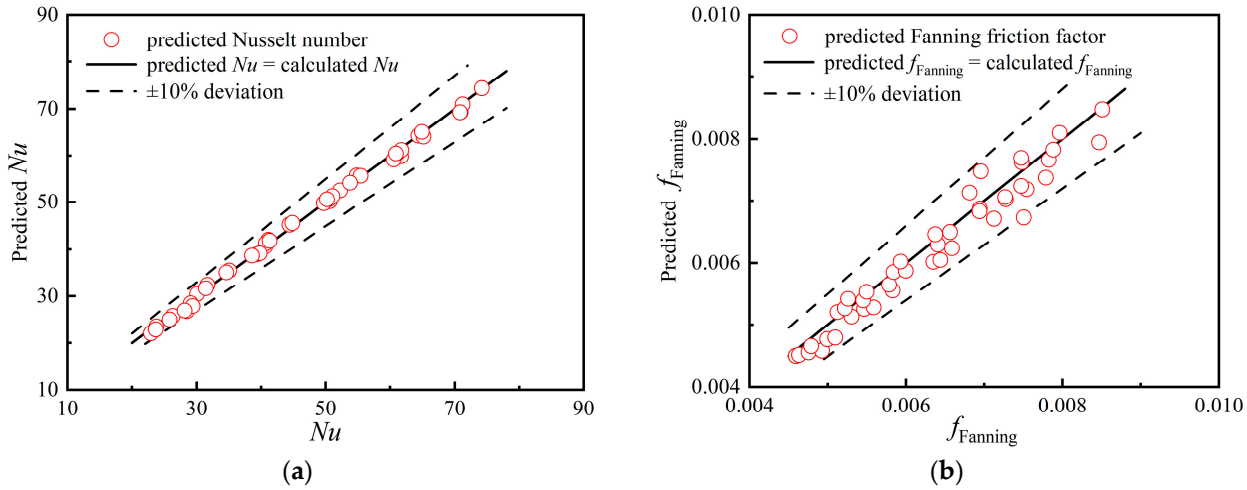



**Figure 15.** Comparison between the correlated predictions and numerical simulations: (**a**) $Nu$ and (**b**) $f_{\text{Fanning}}$.

Selected correlations for $Nu$ and $f$ of existing PCHEs are presented in Table 4. A comparison between the present results and those from previous studies is shown in Figure 16. As this study utilizes transcritical $CH_4$ as the working fluid, variations in the working fluid, heat source, and channel geometry lead to a lower $Nu$ compared to the correlations of Zhao et al. [7] and Park et al. [20]; however, the results exhibit good agreement with those reported by Li et al. [26]. In terms of friction factor prediction, our results align well with those of Park et al. [20] and Zhao et al. [7], while being significantly lower—approximately a quarter of that reported by Li et al. [26].

**Table 4.** Correlations for $Nu$ and $f$ in PCHE channels.

| Author | Channel | Correlation | Fluid |
|---|---|---|---|
| This study | airfoil | $Nu = 0.0002Re^{1.28}Pr^{-2.12}Kb^{-0.17}Ka^{-0.0086}\left(3.96-\lvert 0.11-Ks\rvert^{0.41}\right)^{-0.77}$<br>$f_{\text{Fanning}} = 0.00108Re^{0.166}Pr^{-2.56}Kb^{-0.28}Ka^{-0.12}\left(2.73-\lvert 0.88-Ks\rvert^{0.55}\right)^{-1.37}$<br>$8000 \le Re \le 25,000;\ 1.53 \le Pr \le 1.86$ | $CH_4$ |
| Li et al. [26] | zigzag | $Nu = 0.0087Re^{0.88}Pr^{0.053}\left(\frac{d}{1.4}\right)^{0.098}\left(\frac{\alpha}{15}\right)^{0.31}$<br>$f = 0.06Re^{-0.19}\left(\frac{d}{1.4}\right)^{-0.33}\left(\frac{\alpha}{15}\right)^{1.99}\left(\frac{N}{15}\right)^{0.65}$<br>$14,500 \le Re \le 120,000;\ 1.28 \le Pr \le 1.92$ | $CH_4$ |
| Park et al. [20] | airfoil | $Nu = 0.000241Re^{1.2878}Pr^{0.3}$<br>$f = 0.1354Re^{-0.2832}$<br>$12,000 \le Re \le 30,000;\ 1.29 \le Pr \le 1.59$ | $CO_2$ |
| Zhao et al. [7] | airfoil | $Nu = 0.089163Re^{0.6564}Pr^{0.57616}$<br>$f = -0.0737Re^{0.01937} + 0.09595$<br>$10,000 \le Re \le 55,000;\ 0.76 \le Pr \le 0.80$ | $CH_4$ |

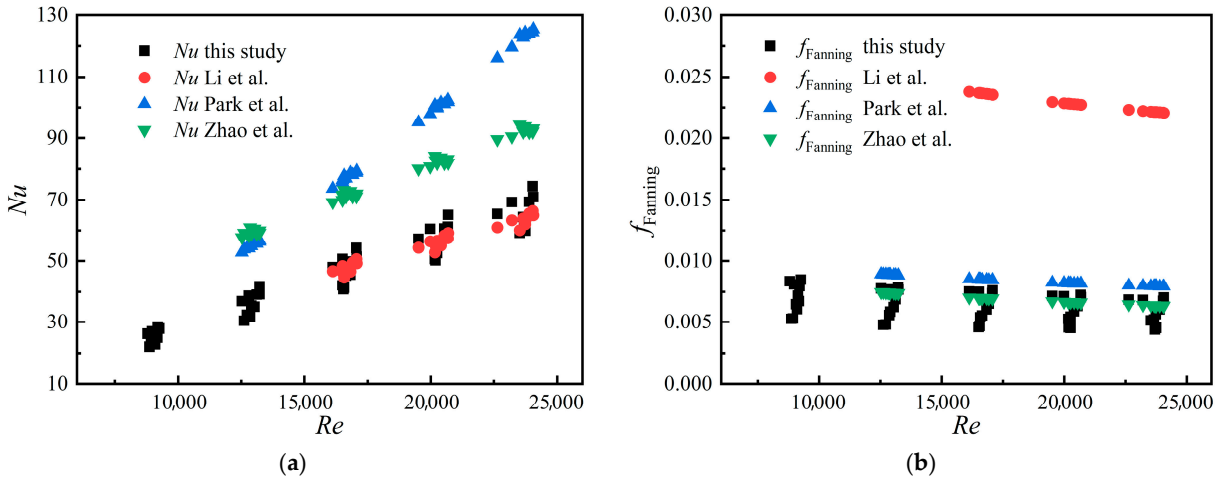



**Figure 16.** Comparison of *Nu* and *f* correlation with those from previous studies: (**a**) *Nu* and (**b**) $f_{\text{Fanning}}$ [7,20,26].

## 5. Conclusions

This study numerically examined the flow and heat transfer behavior of transcritical methane in a PCHE with airfoil fins, systematically assessing the influence of fin arrangement parameters and developing predictive correlations. The key conclusions are as follows:

(1) The airfoil fin arrangement parameters (*Ks*, *Kb*, *Ka*) have a significant and measurable influence on performance. The longitudinal staggering ratio (*Ks*) is identified as a critical factor for balancing heat transfer and flow resistance. An optimal *Ks* value of 0.2 was determined, which promotes fluid disturbance without causing excessive pressure drop. At this configuration and a mass flux of 200 kg·m$^{-2}$·s$^{-1}$, the thermal performance factor (*TPF*) reaches its maximum, achieving a value 1.18 times greater than that of the fully staggered baseline structure (*Ks* = 1.0).

(2) The trade-off between heat transfer enhancement and pressure drop penalty is clearly quantified. Reducing the longitudinal pitch ratio (*Ka*) from 2.0 to 1.0 strengthens turbulent mixing, leading to a significant 13% increase in the Nusselt number (*Nu*). However, this improvement comes at the cost of a 22% increase in the Fanning friction factor ($f_{\text{Fanning}}$), representing a significant pressure drop penalty that must be considered in pump power calculations. Similarly, decreasing the transverse pitch ratio (*Kb*) enhances heat transfer but drastically increases flow resistance, with the most compact arrangement (*Kb* = 0.5) producing the highest *Nu* and $f_{\text{Fanning}}$.

(3) An optimal configuration is identified through a comprehensive evaluation of performance. The fin channel with the parameter combination of *Ks* = 0.2, *Kb* = 0.5, and *Ka* = 1.0 exhibits the best overall thermal-hydraulic performance under a typical engineering mass flux (*G* = 200 kg·m$^{-2}$·s$^{-1}$). This configuration achieves an optimal balance, maximizing the *TPF* by effectively managing the trade-offs between the three geometric parameters.

(4) High-accuracy predictive correlations are developed with defined applicability. Based on extensive simulation data, novel dimensionless correlations were proposed for predicting the *Nu* and $f_{\text{Fanning}}$ values of $sCH_4$ in airfoil-fin PCHEs as follows:

$$Nu = 0.0002Re^{1.28}Pr^{-2.12}Kb^{-0.17}Ka^{-0.0086}\left(3.96 - |0.11 - Ks|^{0.41}\right)^{-0.77}$$

$$f_{\text{Fanning}} = 0.00108Re^{0.166}Pr^{-2.56}Kb^{-0.28}Ka^{-0.12}\left(2.73 - |0.88 - Ks|^{0.55}\right)^{-1.37}$$

These correlations demonstrate high accuracy within the parameter ranges of $Re$ = 8000–25,000, $Pr$ = 1.53–1.86, $Ks$ = 0.0–1.0, $Kb$ = 0.5–0.7, and $Ka$ = 1.0–2.0. The root mean square deviations between predictions and simulations are only 2.08% for $Nu$ and 6.57% for $f_{\text{Fanning}}$, with all data points lying within a 10% deviation band. This provides a highly reliable tool for the design and optimization of PCHEs in $sCH_4$ regasification applications.

**Supplementary Materials:** The following supporting information can be downloaded at: https://www.mdpi.com/article/10.3390/en19020575/s1, UDF Files (Section 3.2).

**Author Contributions:** C.S.: Writing—original draft, Conceptualization, Formal analysis, Investigation, X.M.: Conceptualization, Supervision, Formal analysis, Investigation, Methodology, Writing—review and editing, Y.Z.: Formal analysis, Supervision, L.L.: Investigation, J.Y.: Supervision, Funding acquisition, Writing—review and editing, T.Y.: Funding acquisition, Supervision. All authors have read and agreed to the published version of the manuscript.

**Funding:** This research received no external funding.

**Data Availability Statement:** The original contributions presented in this study are included in the article. Further inquiries can be directed to the corresponding authors.

**Conflicts of Interest:** The authors declare no conflicts of interest.

## Nomenclature

| | |
|---|---|
| $C_p$ | specific heat capacity, $J \cdot kg^{-1} \cdot K^{-1}$ |
| $D_h$ | hydraulic diameter, mm |
| $E_{RMS}$ | root mean square deviation, % |
| $F_1$ | model parameters |
| $f_{\text{Fanning}}$ | Fanning friction factor |
| $G$ | mass flux, $kg \cdot m^{-2} \cdot s^{-1}$ |
| $h$ | heat transfer coefficient, $W \cdot m^{-2} \cdot K^{-1}$ |
| $Ka$ | airfoil fin array longitudinal pitch ratio |
| $Kb$ | airfoil fin array transverse pitch ratio |
| $Ks$ | airfoil fin array longitudinal staggering ratio |
| $L$ | total flow path length, mm |
| $La$ | airfoil fin array longitudinal pitch, mm |
| $Lb$ | airfoil fin array transverse pitch, mm |
| $Lc$ | airfoil chord length, mm |
| $Ld$ | airfoil upper surface perimeter, mm |
| $Lh$ | channel height, mm |
| $Ls$ | airfoil fin array longitudinal staggering |
| $Ln$ | single pitch length, mm |
| $n$ | number of data points |
| $Nu$ | Nusselt number |
| $p$ | pressure, MPa |
| $Pr$ | Prandtl number |
| $q$ | heat flux density, $W \cdot m^{-2}$ |
| $Re$ | Reynolds number |
| $Sa$ | half of the airfoil upper surface area, $mm^2$ |
| $T$ | temperature, K |
| $T_b$ | average fluid temperature in the channel, K |
| $T_W$ | wall temperature, K |
| $\overline{u}$ | mean velocity, $m \cdot s^{-1}$ |
| $\vec{V}$ | velocity vector, $m \cdot s^{-1}$ |
| $X_{num}$ | simulated values |
| $X_{pred}$ | predicted values |

## Greek Symbols

| | |
|---|---|
| $\sigma_\omega$ | model parameters |
| $\sigma_k$ | model parameters |
| $\rho$ | fluid density, kg·m$^{-3}$ |
| $\mu_t$ | turbulent viscosity, Pa·s |
| $\mu$ | dynamic viscosity, Pa·s |
| $\lambda$ | thermal conductivity, W·m$^{-1}$·K$^{-1}$ |
| $\gamma$ | model parameters |
| $\beta^*$ | model parameters |
| $\beta$ | model parameters |
| $\Delta T$ | logarithmic mean temperature difference, K |
| $\Delta p$ | pressure drop, Pa |
| $\Delta p_f$ | frictional pressure drop, Pa |

## Abbreviations

| | |
|---|---|
| FSRU | floating storage and regasification unit |
| LNG | liquefied natural gas |
| NACA | National Advisory Committee for Aeronautics |
| NG | natural gas |
| PCHE | printed circuit heat exchanger |
| *TPF* | the thermal performance factor |
| UDF | user-defined function |

## References


1. Casagrande, S.; Dallago, B. The economic and geostrategic role of LNG in EU energy transition. *Struct. Change Econ. Dyn.* **2025**, *74*, 387–404. [CrossRef]
2. Ji, C.; Yuan, S.; Jiao, Z.; Pettigrew, J.; El-Halwagi, M.M.; Pasman, H.J. Risk informed floating storage and re-gasification unit (FSRU) location selection for local natural gas supply. *Ocean Eng.* **2023**, *268*, 113357. [CrossRef]
3. Bai, J.; Zhang, N.; Liu, X.; Ren, Y.; Yang, J. The sloshing effect on the heat transfer of supercritical LNG in a printed circuit vaporizer on FSRU. *Appl. Therm. Eng.* **2024**, *257*, 124347. [CrossRef]
4. Yoonho, L. LNG-FSRU cold energy recovery regasification using a zeotropic mixture of ethane and propane. *Energy* **2019**, *173*, 857–869. [CrossRef]
5. Yu, K.; Yin, J. Heat transfer analysis of submerged combustion vaporizer under subcritical pressure and comparison with supercritical pressure. *Cryogenics* **2021**, *120*, 103372. [CrossRef]
6. Sun, J.; Xie, G.; Zhao, D.; Jin, P.; Duan, Z. Comparative thermodynamic and frictional characteristics of supercritical LNG in a PCHE with teardrop dimples and protrusions under single and coupled rolling-heaving ocean motions. *Ocean Eng.* **2025**, *333*, 121484. [CrossRef]
7. Zhao, C.; Wang, Y.; Yang, L.; Zhao, B.; Li, Q.; Cai, W. Numerical study on flow and heat transfer characteristics of supercritical methane in microchannels with airfoil fins. *J. Supercrit. Fluids* **2025**, *222*, 106596. [CrossRef]
8. Zhong, S.; Ren, Y.; Wang, P.; Wu, W.; Yang, Y.; Yang, Q. Experimental test of rectangular microchannel printed circuit heat exchanger using supercritical carbon dioxide as working fluid. *J. Supercrit. Fluids* **2023**, *200*, 105967. [CrossRef]
9. Li, Q.; Fu, X.; Lin, Z.; Liu, X.; Zhao, B.; Cai, W. Analysis of complex methane transcritical flow and heat transfer mechanism in PCHE Zigzag channel. *Int. J. Therm. Sci.* **2025**, *210*, 109678. [CrossRef]
10. Zhao, Z.; Zhou, Y.; Ma, X.; Chen, X.; Li, S.; Yang, S. Numerical Study on Thermal Hydraulic Performance of Supercritical LNG in Zigzag-Type Channel PCHEs. *Energies* **2019**, *12*, 548. [CrossRef]
11. Cai, W.; Li, Y.; Li, Q.; Wang, Y.; Chen, J. Numerical investigation on thermal–hydraulic performance of supercritical LNG in a Zigzag mini-channel of printed circuit heat exchanger. *Appl. Therm. Eng.* **2022**, *214*, 118760. [CrossRef]
12. Liu, K.; Zhao, F.; Jin, Y.; Hu, C.; Ming, Y.; Liu, Y.; Tian, R.; Liu, S. S–$CO_2$ heat transfer characteristics analysis in PCHE and vertical channel. *Prog. Nucl. Energy* **2022**, *154*, 104472. [CrossRef]
13. Jin, F.; Yuan, D.; Chen, D.; Hu, L.; Huang, Y.; Bu, S. Experimental study on cooling heat transfer performance of supercritical $CO_2$ in zigzag printed circuit heat exchanger. *Int. J. Heat Mass Transfer* **2023**, *215*, 124538. [CrossRef]
14. Liu, B.; Lu, M.; Shui, B.; Sun, Y.; Wei, W. Thermal-hydraulic performance analysis of printed circuit heat exchanger precooler in the Brayton cycle for supercritical $CO_2$ waste heat recovery. *Appl. Energy* **2022**, *305*, 117923. [CrossRef]

15. Wang, Y.; Ren, J.; Gao, W.; Zhang, J.; Yu, G.; Bi, M. Mechanism analysis on heat transfer of supercritical LNG in horizontal U-bend tube. *Energy* **2024**, *304*, 131936. [CrossRef]
16. Li, Y.; Li, Q.; Wang, Y.; Chen, J.; Cai, W. Optimization of a Zigzag-channel printed circuit heat exchanger for supercritical methane flow. *Cryogenics* **2022**, *121*, 103415. [CrossRef]
17. Ma, T.; Zhang, P.; Deng, T.; Ke, H.; Lin, Y.; Wang, Q. Thermal-hydraulic characteristics of printed circuit heat exchanger used for floating natural gas liquefaction. *Renew. Sustain. Energy Rev.* **2021**, *137*, 110606. [CrossRef]
18. Tang, L.-H.; Yang, B.-H.; Pan, J.; Sundén, B. Thermal Performance Analysis in a Zigzag Channel Printed Circuit Heat Exchanger under Different Conditions. *Heat Transfer Eng.* **2021**, *43*, 567–583. [CrossRef]
19. Li, Q.; Zhan, Q.; Yu, S.; Sun, J.; Cai, W. Study on thermal-hydraulic performance of printed circuit heat exchangers with supercritical methane based on machine learning methods. *Energy* **2023**, *282*, 128711. [CrossRef]
20. Park, J.H.; Kim, M.H. Experimental investigation on comprehensive thermal-hydraulic performance of supercritical $CO_2$ in a NACA 0020 airfoil fin printed circuit heat exchanger. *Int. J. Heat Mass Transfer* **2024**, *220*, 124947. [CrossRef]
21. Liu, W.; Xu, G.; Zhi, H.; Wang, R.; Li, M.; Fu, Y. Experimental evaluation of hydrothermal performance in airfoil-fin PCHE with supercritical pressure hydrocarbon fuel. *Int. Commun. Heat Mass Transfer* **2024**, *159*, 108279. [CrossRef]
22. Li, Y.; Fu, Y.; Zhang, J.; Zhang, J.; Xu, J.; Ma, S.; Sunden, B.; Xie, G. Investigation of heat transfer performance and enhancement mechanisms of supercritical carbon dioxide in PCHE with fractal airfoil fins. *Case Stud. Therm. Eng.* **2024**, *60*, 104802. [CrossRef]
23. Pidaparti, S.R.; Anderson, M.H.; Ranjan, D. Experimental investigation of thermal-hydraulic performance of discontinuous fin printed circuit heat exchangers for supercritical $CO_2$ power cycles. *Exp. Therm. Fluid Sci.* **2019**, *106*, 119–129. [CrossRef]
24. Arora, O.; Cosials, K.F.; Vaghetto, R.; Hassan, Y.A. Pressure drop and friction factor study for an airfoil-fin printed circuit heat exchanger using experimental and numerical techniques. *Int. J. Heat Fluid Flow* **2023**, *101*, 109137. [CrossRef]
25. Han, Z.; Cui, X.; Guo, J.; Zhang, H.; Zhou, J.; Cheng, K.; Zhang, H.; Huai, X. Experimental and numerical studies on the thermal-hydraulic performance of a novel airfoil fins printed circuit heat exchanger. *Int. J. Heat Mass Transfer* **2023**, *217*, 124655. [CrossRef]
26. Li, L.; Wu, J.; Yin, J. Geometry Optimization and Performance Prediction of Printed Circuit Heat Exchanger for Supercritical Methane. *J. Therm. Sci.* **2025**, *34*, 1953–1963. [CrossRef]
27. Yang, L.; Zhang, R.; Zhang, G.; Zhao, B.; Li, Q.; Cai, W. Study on data universality and machine learning for methane transcritical flow and heat transfer in PCHE channel with different boundary conditions. *J. Supercrit. Fluids* **2025**, *225*, 106700. [CrossRef]
28. Jiang, T.; Li, M.; Wang, W.; Li, D.; Liu, Z. Fluid-Thermal-Mechanical Coupled Analysis and Optimized Design of Printed Circuit Heat Exchanger with Airfoil Fins of S-$CO_2$ Brayton Cycle. *J. Therm. Sci.* **2022**, *31*, 2264–2280. [CrossRef]
29. Kim, I.H.; No, H.C.; Lee, J.I.; Jeon, B.G. Thermal hydraulic performance analysis of the printed circuit heat exchanger using a helium test facility and CFD simulations. *Nucl. Eng. Des.* **2009**, *239*, 2399–2408. [CrossRef]
30. Zhao, Z.; Zhang, Y.; Chen, X.; Ma, X.; Yang, S.; Li, S. Experimental and numerical investigation of thermal-hydraulic performance of supercritical nitrogen in airfoil fin printed circuit heat exchanger. *Appl. Therm. Eng.* **2020**, *168*, 114829. [CrossRef]
31. Lemmon, E.W.; Huber, M.L.; McLinden, M.O. *NIST Standard Reference Database 23: Reference Fluid Thermodynamic and Transport Properties Database (REFPROP), Version 9.1*; Standard Reference Database 23; National Institute of Standards and Technology: Gaithersburg, MD, USA, 2013. [CrossRef]
32. Webb, R.L. Performance evaluation criteria for use of enhanced heat transfer surfaces in heat exchanger design. *Int. J. Heat Mass Transfer* **1981**, *24*, 715–726. [CrossRef]
33. Babaelahi, M.; Raveshi, M.R. Analytical efficiency analysis of aerospace radiating fin. *Proc. Inst. Mech. Eng. Part C J. Mech. Eng. Sci.* **2014**, *228*, 3133–3140. [CrossRef]
34. Zhao, Z.; Zhao, K.; Jia, D.; Jiang, P.; Shen, R. Numerical Investigation on the Flow and Heat Transfer Characteristics of Supercritical Liquefied Natural Gas in an Airfoil Fin Printed Circuit Heat Exchanger. *Energies* **2017**, *10*, 1828. [CrossRef]


**Disclaimer/Publisher's Note:** The statements, opinions and data contained in all publications are solely those of the individual author(s) and contributor(s) and not of MDPI and/or the editor(s). MDPI and/or the editor(s) disclaim responsibility for any injury to people or property resulting from any ideas, methods, instructions or products referred to in the content.